Hybrid Integration of GaP Photonic Crystal Cavities with Silicon-Vacancy Centers in Diamond by Stamp-Transfer

Srivatsa Chakravarthi, Nicholas S. Yama,* Alex Abulnaga, Ding Huang, Christian Pederson, Karine Hestroffer, Fariba Hatami, Nathalie P. de Leon, and Kai-Mei C. Fu

ABSTRACT: Optically addressable solid-state defects are emerging as some of the most promising qubit platforms for quantum networks. Maximizing photon-defect interaction by nanophotonic cavity coupling is key to network efficiency. We demonstrate fabrication of gallium phosphide 1-D photonic crystal waveguide cavities on a silicon oxide carrier and subsequent integration with implanted silicon-vacancy (SiV) centers in diamond using a stamp-transfer technique. The stamping process avoids diamond etching and allows fine-tuning of the cavities prior to integration. After transfer to diamond, we measure cavity quality factors (Q) of up to 8900 and perform resonant excitation of single SiV centers coupled to these cavities. For a cavity with a Q of 4100, we observe a 3-fold lifetime reduction on-resonance, corresponding to a maximum potential cooperativity of $C = 2$. These results indicate promise for high photon-defect interaction in a platform which avoids fabrication of the quantum defect host crystal.

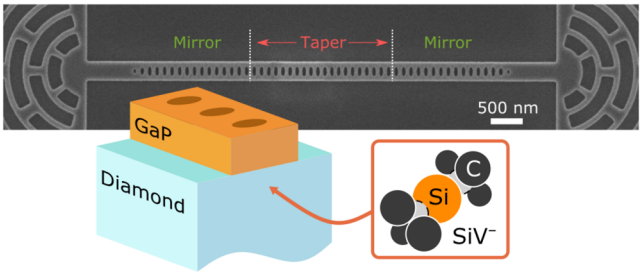

KEYWORDS: *silicon-vacancy center, hybrid cavity, gallium phosphide, Purcell enhancement*

In an optical quantum network, quantum entanglement is distributed among spatially separated stationary qubit nodes through flying qubits (photons),[1] enabling long-range quantum communication[2] and distributed quantum computing.[3] Optically addressable defects[4] in materials like diamond,[5,6] silicon carbide,[7,8] ZnO,[9] and rare-earth doped crystals[10,11] show tremendous potential for realization of such stationary qubit nodes. For defect qubits, efficient generation and utilization of intermediary photon qubits can be enabled by on-chip photonic integration of defect qubits. Here, we demonstrate a hybrid-photonic architecture in diamond, integrating single negatively charged silicon-vacancy qubits with waveguide integrated gallium phosphide (GaP) photonic crystal (PhC) cavities.[12]

Negatively charged silicon-vacancy (SiV) centers in high-quality diamond crystals show nearly lifetime-limited optical transitions for centers created by ion-implantation and vacuum annealing.[13] The favorable spectral behavior of the SiV center can be attributed to its inversion symmetry, which protects the optical transitions from electric field noise in the environment.[14,15] This protection has enabled high-cooperativity coupling of SiV centers to monolithic diamond photonic structures,[16] which has resulted in significant breakthroughs in the development of quantum repeaters[17] and on-chip entanglement.[18] While such results are promising, the necessity of etching bulk diamond is both practically challenging and potentially damaging to defect properties due to fabrication-induced surface states.[19,20]

Here we explore an alternative hybrid planar geometry that eliminates diamond etching, thus minimizing fabrication-induced damage to the defect environment that could result in degraded spectral stability. This is enabled by the choice of GaP as the waveguiding medium owing to its high refractive index ($n_{GaP} = 3.24$) and large band gap (2.24 eV). Photonic cavities are fabricated on an intermediate GaP on silicon oxide carrier chip and then transferred to a diamond sample with implanted SiV defects via a polymer-stamping process.[12,21] In contrast to prior bulk diamond hybrid systems,[22,23] our process completely eliminates all diamond etching. Furthermore, the hybrid stamp transfer process will allow for the selection and fine-tuning of promising SiV and PhC cavities separately prior to integration to improve yield and performance simultaneously. Commercial wafer-scale implementations of stamp-transfer pick-and-place hybrid photonic integration processes[24−26] and access to the strong nonlinear and optomechanical properties of GaP suggest good prospects for

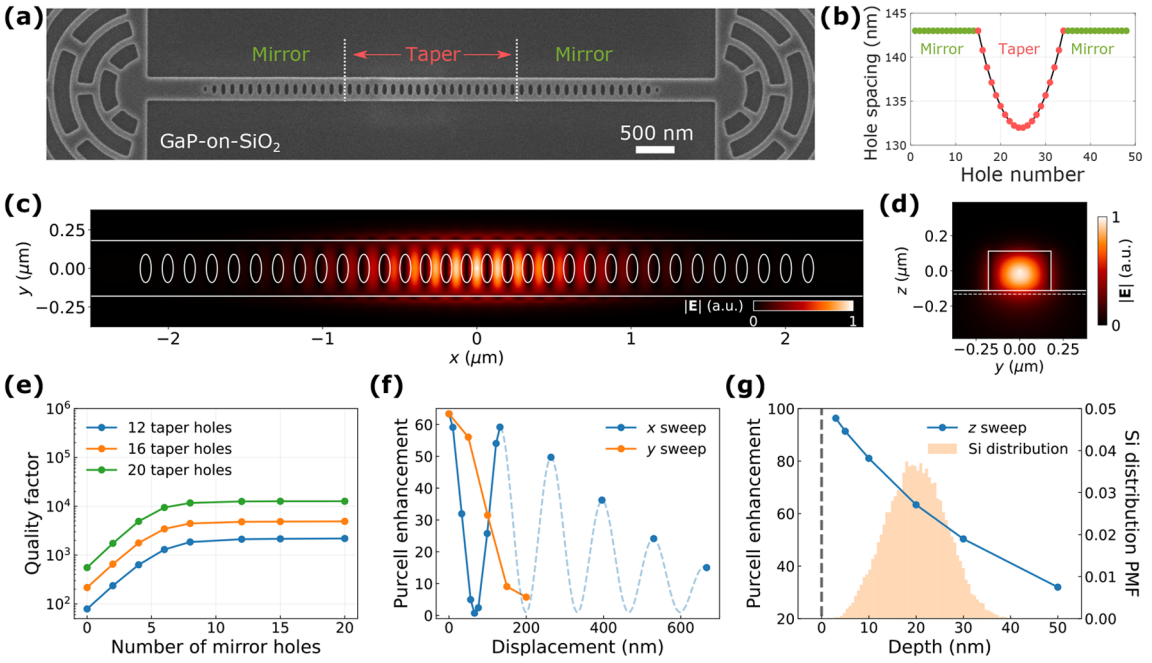

Figure 1. (a) SEM image of a representative 1-D GaP cavity. (b) Variation of the hole spacing across the cavity, distinguishing the mirror and taper regions. (c, d) Simulated E-field intensity of the cavity mode of the measured device across the *xy*-plane ((c) $z = 0$ centered on GaP layer) and *yz*-plane ((d) $x = 0$ centered on cavity maxima) within the GaP-on-diamond structure. The dashed line in (d) corresponds to the mean SiV position. (e) Simulated scaling of the total *Q* factor of the GaP-on-diamond cavity with increasing number of mirror and taper holes. (f, g) Simulated Purcell enhancement for a dipole oriented with 90° polar and 54.736° azimuth angles with respect to the cavity axis (corresponding to an optimally aligned ⟨111⟩ dipole). In (f) the dipole is positioned 20 nm below the GaP−diamond interface and displaced from the cavity maxima ($x = y = 0$) in the *xy*-plane. The points are individual simulations with the dashed line for the *x* sweep being a guide to the eye for an approximate variation. In (g) the dipole is positioned at $x = y = 0$ and swept vertically within the diamond. A simulated probability distribution of the implanted Si atoms is shown on the right-side axis which is centered at 20 nm beneath the surface.

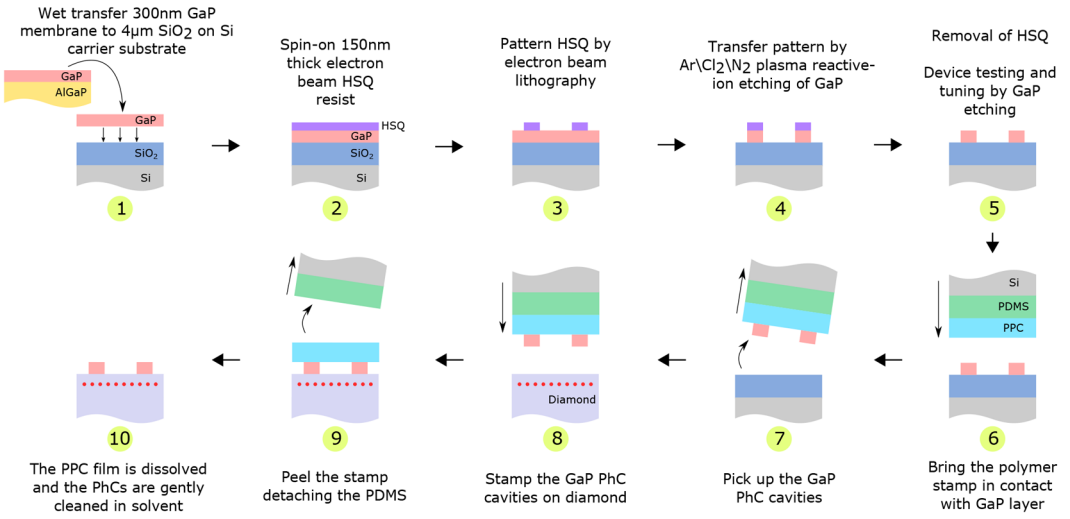

Figure 2. Illustration of the stamp transfer process. We begin with GaP cavities fabricated on a silicon oxide carrier chip and finish with cavities integrated with implanted SiV centers in a host diamond chip. Microscope images from various stages of fabrication are provided in SI.2.

scalable assembly of defect−cavity interfaces with visible-to-telecom frequency conversion[27] and microwave-to-optical transduction[28] devices.

We demonstrate single SiV qubits coupled to GaP photonic cavities. We observe a quality factors on the silicon oxide carrier exceeding $Q_{SiO_2} = 30000$ and up to $Q_{Dia} = 8900$ after stamp transfer to the diamond substrate. For a cavity with $Q_{Dia} = 4100$ we see a 3-fold reduction in the coupled SiV lifetime with the cavity on-resonance. The observed lifetime reduction corresponds to a minimum cavity Purcell enhancement of 30 and a maximum possible cooperativity of 2 for the coupled SiV center.

The device consists of a 1-D array of elliptical holes etched into the GaP (Figure 1a). The designed GaP layer thickness is constrained to 222 nm. A unit cell of the cavity consists of a single elliptical hole with major axis h_y and minor axis h_x, GaP width w, and lattice constant a_{cav}. The cavity can be divided into the taper and mirror sections as shown in Figure 1b.

Within the mirror region, the hole periodicity, a_{mir}, is chosen to maximize the TE quasi-band gap around the target frequency of the SiV zero-phonon transition at 737 nm. Within the taper region, the hole periodicity is adiabatically reduced from a_{mir} so as to create a defect mode for the target frequency. The presence of the high-index diamond substrate underneath the GaP introduces design challenges toward achieving high Q because the substrate expands the light-line such that photons can couple to the continuum of modes in the diamond and thus leak out of the cavity. Full details of the cavity design and optimization can be found in refs 12 and 29.

We restrict the minimum feature size to be 70 nm due to fabrication limitations. The optimized design, with (a_{mir}, a_{cav}, h_x, h_y, w) = (140, 133, 71, 183, 360) nm, is simulated using a finite-difference time-domain method (FDTD, Lumerical). A driven dipole source modeling the SiV is placed within the evanescent cavity field. The time-decay of the cavity mode and measured radiated power are utilized to estimate the resonator characteristics and tolerance to dipole placement (Figure 1c–g; see SI.7 for details). For a defect 20 nm beneath the GaP–diamond interface a Purcell enhancement as high as 60 is possible, which increases to 95 at 3 nm beneath the interface.

The cavity structure is fabricated using a 300 nm GaP membrane (Figure 2, steps 1–5) that is released from a GaP substrate by etching an intermediate $Al_{0.8}Ga_{0.2}P$ sacrificial layer with dilute HF. The GaP membrane is then transferred to a silicon oxide on Si substrate using a wet-transfer process.[23,30,31] Electron-beam lithography is performed using a hydrogen silsesquioxane (HSQ) resist to pattern the cavity devices. Subsequent inductively coupled plasma reactive-ion-etching (RIE) of the GaP layer forms the photonic devices.

The GaP-on-oxide cavity devices are characterized before stamp transfer to diamond. The resonances of individual devices are identified by using a supercontinuum laser (600–800 nm; see SI.1) to obtain the transmission spectra. The excitation is linearly polarized and matched to the TE resonator mode. Scattered excitation light was filtered from the collection path via spatial filtering. We measure cavity resonances near 770 nm (Figure 3a-1) which are red-shifted from the design due to the thicker initial GaP height of 300 nm (design specification is 222 nm). This enables fine-tuning of the resonance by blanket etching and improves robustness against random fabrication imperfections.

The cavity resonance needs to be centered around the SiV ZPL wavelength of 737 nm when it is transferred to diamond. We target 731 nm on the SiO_2 carrier chip, as the higher-index diamond is expected to red-shift the resonances by ∼7 nm. We blue-shift the cavity resonances by iterative thinning of the GaP layer (Figure 3a: spectra 1–5) using a blanket GaP RIE plasma etch (15 s for step 1, 8 s for steps 2–5; GaP etch rate ∼100 nm/min). After each etch cycle, the GaP-on-oxide cavity transmission is measured to track the resonance blue-shift. After thinning, many cavities exhibit quality factors at the spectrometer limit (Q_{SiO_2} > 30000). We measure a final GaP thickness of 225 nm (SI.2) and do not observe a significant change to the hole dimensions as a result of the thinning process. Note that without the stamping process, this step could have introduced damage to the diamond surface, potentially affecting near-surface SiV.

A chemical vapor deposition diamond (Element Six, electronic grade, N < 5 ppb, B < 1 ppb, surface orientation (100)) is implanted with Si accelerated to 26 keV (5e11 cm^{-2} dose, 7° angle) and vacuum annealed at 1200 °C for 2 h. During annealing, SiV centers are formed by vacancy diffusion and recombination with the implanted silicon, yielding a layer of SiV centers 20 nm from the surface (∼50 SiV centers per ∼800 nm diameter excitation spot).

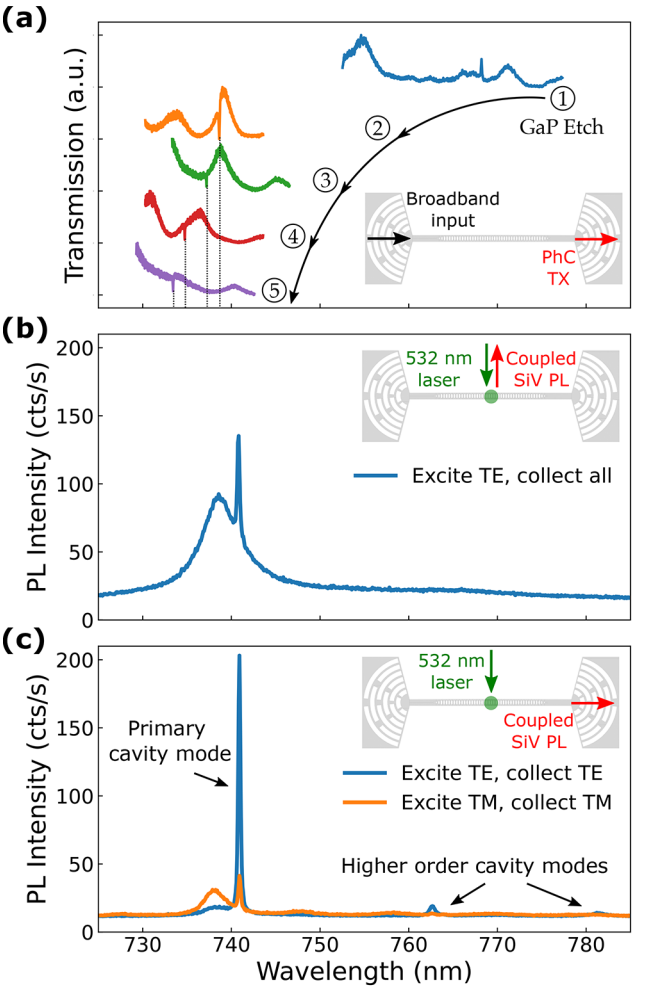

Figure 3. RT measurements. (a) Transmission spectra of one specific GaP-on-SiO_2 cavity tracked through multiple GaP thinning plasma etch cycles. The resonance is blue-shifted from 769 to 733 nm as the GaP thickness is reduced. (b) Spectra of a GaP-on-diamond cavity with the excitation and PL collection at the center of the cavity. The ensemble SiV PL can be observed with a sharp peak at 741 nm indicating the cavity mode. This configuration enables the collection of PL outside of the cavity bandwidth which is necessary for resonant excitation measurements. (c) Spectra of a GaP-on-diamond cavity with grating-coupled PL collection. The cavity mode is significantly brighter and exhibits strong polarization preference for TE collection (matching the designed TE cavity mode).

To transfer the cavities to the diamond, a stamping procedure[29,32] is utilized, as shown in (Figure 2, steps 6–10). The process is carried out in a flip-chip wafer-bonder which controls both pressure and temperature. The process uses a PDMS stamp fabricated into a mesa structure and an intermediate polypropylene carbonate (PPC) film. The PDMS/PPC stack is brought in contact with the devices and heated to 60 °C to promote adhesion. Next, the PDMS/PPC/cavity stack is lifted off the carrier substrate. The diamond substrate is cleaned in a piranha solution bath (H_2SO_4:H_2O_2 = 3:1) prior to stamping. The PDMS/PPC/cavity stack is

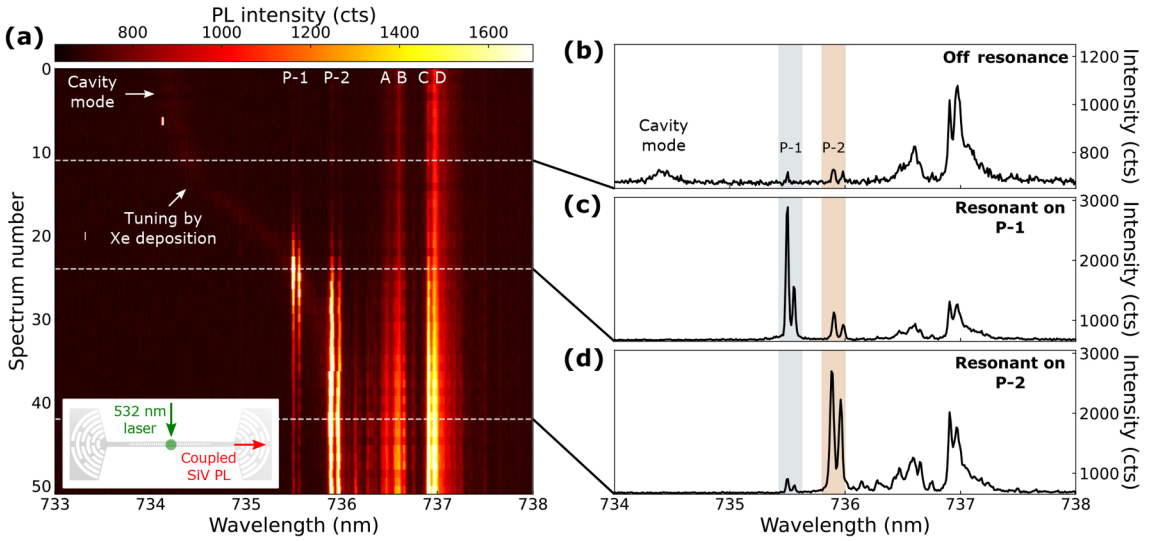

Figure 4. LT 10 K cavity tuning. (a) Sequence of spectra (60 s exposures) showing the cavity mode red-shifting from xenon gas deposition with a maximum tuning range of ~1.9 nm. The cavity is tuned through two SiV ZPL pairs (P-1, P-2). Inset: illustration of the measurement geometry with the 532 nm excitation at the cavity and grating-coupled SiV PL collection. (b) Spectra of the cavity off-resonance. (c, d) Spectra of the cavity on-resonance with P-1 (c) and P-2 (d). The blue and orange boxes indicate the filtering windows utilized for on-resonance lifetime measurements.

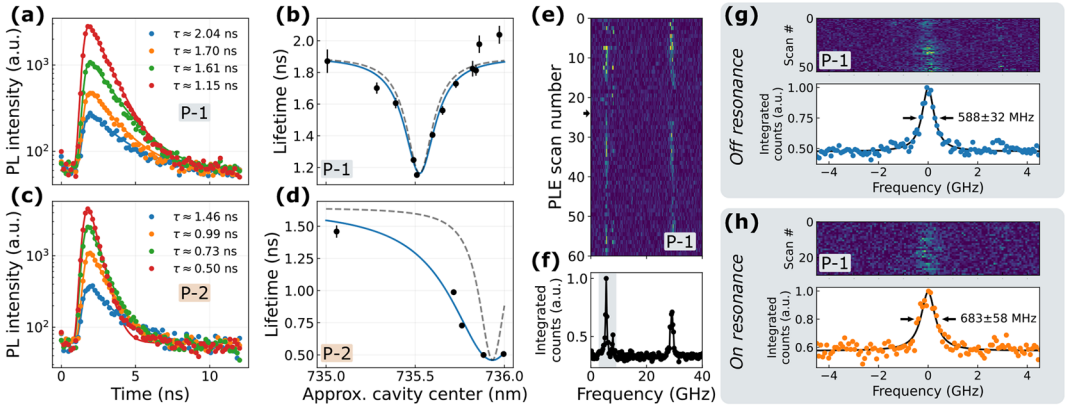

Figure 5. LT 10 K measurements. Time-resolved PL and extracted excited-state lifetime of SiV pairs (a, b) P-1 and (c, d) P-2 as a function of cavity detuning. We observe enhancements of the decay rate by factors of 1.7 ± 0.1 and 3.0 ± 0.1 for P-1 and P-2, respectively. A Lorentzian fit (blue) to the lifetime data results in a line width that is broader than the cavity line width (dashed grey). (e) PLE scans on ZPL P-1 when the cavity is significantly red detuned. Each scan is taken over 2 s and repeated at 10 s intervals. After each scan, a 532 nm pulse was occasionally used to reset the SiV charge state if ionization occurred; one such instance is indicated by the black arrow at scan 24. (f) Integrating all scans in (e) shows two bright lines separated by around 25 GHz approximately corresponding to the spacing observed in spectra. The highlighted line near 5 GHz is further examined by tuning the cavity from (g) off-resonance to (h) on-resonance while continuously performing PLE scans. The line width is observed to broaden by 95 ± 66 MHz when the cavity is tuned on-resonance, which is approximately consistent with an enhancement of 1.7 of the decay rate.

aligned to the diamond edge (⟨110⟩) and pressed down on the diamond substrate. The stamp and diamond are heated to 130 °C, which softens the PPC layer to release the PPC film from the PDMS stamp. Finally, we dissolve the PPC in trichloroethylene and soak the diamond in acetone followed by IPA.

Following the GaP transfer to diamond, we observe resonances for all 28 intact transferred cavities, with resonance wavelengths in the range of 730−755 nm. Remarkably, many stamped devices show cavity resonances with quality factors as high as 8900, close to the simulated design value of 10000 (SI.3.).

Room-temperature photoluminescence (PL) measurements are performed to study SiV coupling to the stamped GaP photonic devices. We excite with an off-resonant 532 nm laser and collect SiV PL normal to the sample at the excitation position (Figure 3b). At room temperature, the SiV PL spectrum consists of a zero-phonon line (ZPL) at 738 nm (full-width at half-maximum (fwhm) of 5 nm) and a broad phonon sideband (PSB) (744−800 nm). We observe increased SiV ZPL emission at the cavity resonance along with a significant background ZPL contribution from other SiV centers within the excitation spot. By collecting the SiV PL coupled into the waveguide at the output grating, we observe a significantly larger fraction of SiV ZPL intensity at the cavity resonance with minimal background SiV contribution (Figure 3c). Further, we observe a clear polarization dependence for the coupled SiV PL consistent with the designed TE cavity mode. These results confirm coupling of the implanted SiV and the stamped GaP PhC cavity.

When the devices are cooled to 10 K, their cavity modes are blue-detuned from room temperature by ∼5.5 nm due to the temperature dependence of the GaP index. Utilizing the 532 nm off-resonant excitation at the cavity center, we can monitor the cavity mode and SiV ZPL transitions at the output grating. A typical spectrum shows four bright lines near 737 nm corresponding to the characteristic A−D transitions for SiV,[14] together with a number of faint detuned lines associated with strained single SiV centers. The cavity mode can be red-shifted by injecting xenon gas into the sample chamber. The xenon condenses on the sample, increasing the effective index of the cavity mode and resulting in a controlled resonance shift as demonstrated in Figure 4a. The maximum range of the xenon-induced red-shift is 1.9 nm. Although all 28 intact devices from the stamped array exhibit cavity resonances, only the nine devices having resonances within 3 nm of 737 nm are utilized for xenon tuning measurements. For all nine devices, we are able to observe a significant increase in PL on-resonance for a range of SiV transitions from blue to red detuned with respect to the ensemble A−D lines (Figure 4a; see other devices in SI.4).

To facilitate coupling to single SiV transitions and for ease of cavity-mode identification, we focus on a device with isolated blue-detuned SiV transitions. We select a device with Q_{Dia} = 4100 which exhibits the maximum increase in PL of all devices. For this device, the cavity mode is tuned through two pairs of SiV ZPL denoted P-1 and P-2 (Figure 4). In order to quantify the SiV−cavity coupling we first perform time-resolved PL measurements while tuning the cavity over P-1 and P-2. We excite at the cavity with pulsed excitation at 704 nm (500 μW average power, 2 ps pulse width, and 80 MHz repetition rate) and collect PL through the output grating, thus filtering only the cavity-coupled SiV. We then spectrally filter the PL via a spectrometer (0.2 nm bandwidth, centered on P-1 or P-2) and detect the PL with an avalanche photodiode. A low-intensity continuous-wave (20 μW) 532 nm laser is added to help stabilize the negative SiV charge state (SI.6). By fitting the temporally resolved PL[33] (Figure 5a,c; see SI.8 for details), we observe a reduction of the lifetime on resonance by a factor of

$$\frac{\tau^{\text{P-1}}_{\text{off-res}}}{\tau^{\text{P-1}}_{\text{on-res}}} = 1.77 \pm 0.02 \qquad \frac{\tau^{\text{P-2}}_{\text{off-res}}}{\tau^{\text{P-2}}_{\text{on-res}}} = 2.92 \pm 0.07$$

A plot of the lifetime as a function of cavity detuning (Figure 5b,d) exhibits a Lorentzian line shape, with a line width that is broader than the cavity resonance. This is consistent with the theory (SI.7) and potential broadening due to the two transitions comprising each pair (with separationz of about 0.06 and 0.08 nm for P-1 and P-2, respectively).

Next, we perform photoluminescience excitation (PLE) spectroscopy to characterize the optical line widths off and on cavity resonance. The SiV is resonantly excited via a low-power tunable diode laser which is scanned over the ZPL transition under consideration while the phonon sideband PL is collected (λ > 760 nm) from above the cavity (as this emission is not resonant with the cavity). We observe distinct and consistent lines corresponding to ZPL P-1 (Figure 5e−h) and P-2 (SI.5) by exciting either through the input grating or directly on the cavity. To maintain constant excitation intensity at the SiV during the scan, we select the latter configuration. Between different SiV centers, the excitation power was varied from 100 nW to 1 μW to optimize the signal-to-noise while minimizing SiV ionization. Additionally, a low-intensity blue LED and/or 532 nm pulse enabled consistent repumping of the SiV (SI.5).

We focus on ZPL P-1 due to the larger tuning range of the cavity. Figure 5e shows a series of PLE scans over ZPL P-1 with the cavity red detuned by approximately 0.7 nm. Two bright lines are observed to be separated by about 25 GHz, consistent with the separation measured in PL. The off-resonant lifetime of ZPL P-1 measured in Figure 5a was determined to be $\tau^{\text{P-1}}_{\text{off-res}} = 2.04 \pm 0.06$ ns which corresponds to a lifetime-limited line width $1/2\pi\tau^{\text{P-1}}_{\text{off-res}} = 78 \pm 2$ MHz. The additional broadening of the lines is understood to be a result of a combination of the homogeneous phonon-broadening (limit of ∼250 MHz at 10 K[34]) and spectral diffusion. Because the broadening due to pure lifetime reduction is expected to be $(1/2\pi\tau^{\text{P-1}}_{\text{on-res}}) - (1/2\pi\tau^{\text{P-1}}_{\text{off-res}}) = 60$ MHz, we focus on the highlighted line near 5 GHz, as it is significantly narrower than the other line near 30 GHz. While performing PLE scans centered on this line, we tune the cavity from the original red-detuned position into resonance (Figure 5g,h). We measure a modest broadening of the overall line width by $\Delta\Gamma/2\pi = 95 \pm 66$ MHz, which is consistent with the estimated broadening via the lifetime measurements.

The lifetime and line width measurements can be utilized to determine the Purcell enhancement and cooperativity of the SiV−cavity system. The SiV−cavity system can be modeled as an open system where the cavity is a purely additive decay channel with cavity loss rates $\kappa \equiv \omega/Q$ and defect loss rates γ (including both radiative and nonradiative channels outside of the cavity). A Jaynes−Cummings Hamiltonian with single-photon Rabi frequency g describes the SiV−cavity interaction (SI.7). If we consider only contributions to γ which describe population decay (i.e., ignore pure dephasing) and assume that the system is in the "bad-cavity" regime ($\kappa \gg g, \gamma$), we may define the Purcell enhancement F as the multiplicative increase in the decay rate of the coupled transition:[35]

$$F \equiv 1 + F_{\mathrm{p}}\left(\frac{\vec{\mathbf{E}}\cdot\vec{\mu}}{|\vec{\mathbf{E}}_{\max}||\vec{\mu}|}\right)^2 \frac{(\kappa/2)^2}{(\kappa/2)^2 + \delta^2} \tag{1}$$

Here $\vec{\mathbf{E}}/|\vec{\mathbf{E}}_{\max}|$ is the unit-normalized mode electric-field profile, δ is the SiV-cavity (angular) frequency detuning, and $\vec{\mu}/|\vec{\mu}|$ is a unit vector in the direction of the transition's dipole moment. The constant $F_{\mathrm{p}} \equiv (3/4\pi^2)(\lambda/n)^3(Q/V)$ is the well-known Purcell factor for a cavity with mode volume V at wavelength λ/n.[36]

Further assuming that the emitter's proximity to the cavity does not substantially modify γ, we can determine the ratio of the off-resonant ($\delta \to \infty$) and on-resonant ($\delta = 0$) lifetimes τ to be given by

$$\frac{\tau_{\text{off-res}}}{\tau_{\text{on-res}}} = 1 + \frac{4g^2}{\kappa\gamma} \tag{2}$$

Comparing eq 2 to eq 1 enables estimation of the resonant Purcell enhancement F_0 via the relation

$$F_0 = 1 + \frac{\gamma}{\gamma_{\mathrm{eg}}}\left(\frac{\tau_{\text{off-res}}}{\tau_{\text{on-res}}} - 1\right) \tag{3}$$

where γ_{eg} is intrinsic spontaneous emission rate of the relevant transition. The factor $\gamma/\gamma_{\mathrm{eg}}$ is an intrinsic (cavity-independent) property of the emitter and may be estimated from the quantum efficiency η, Debye−Waller factor DW, and ZPL

branching ratio ξ as $\gamma/\gamma_{eg} = (\eta \cdot DW \cdot \xi)^{-1}$ (SI.7). Taking upper-bound estimates of $\eta = 0.3$,[37] $DW = 0.7$,[38] and $\xi = 0.325$[39] provides a lower bound on $(\gamma/\gamma_{eg})_{min} \approx 14.65$, which gives a lower bound on the Purcell enhancement $F_{0,min}$ of P-1 and P-2. Using the measured lifetime data (Figure 5) we find

$$F_{0,min}^{P\text{-}1} \approx 12 \quad F_{0,min}^{P\text{-}2} \approx 29$$

which are within the range of feasible Purcell enhancement (Figure 1f,g).

Additionally, the cooperativity C of the SiV-cavity system can be defined as $C \equiv 4g^2/\kappa(\gamma + \gamma_d)$, where γ_d is the pure-dephasing rate. Using the total off-resonant line width $(\gamma + \gamma_d)/2\pi = 588 \pm 32$ MHz and lifetime-limited line width $\gamma/2\pi = 82.0 \pm 0.4$ MHz, we are able to estimate the cooperativity of the P-1 transition under consideration as

$$C^{P\text{-}1} = \frac{\gamma}{\gamma + \gamma_d}\left(\frac{\tau_{off\text{-}res}}{\tau_{on\text{-}res}} - 1\right) = 0.10 \pm 0.01 \quad (4)$$

Reducing the temperature to eliminate the thermal photon broadening beyond the lifetime limit is expected to reduce the total line width to $(\gamma + \gamma_d)/2\pi \approx 420$ MHz. Provided the other broadening mechanisms are temperature independent, this would result in a cooperativity of $C_{0\,K}^{P\text{-}1} \approx 0.14$. If the SiV line width is lifetime limited (i.e., no pure dephasing), then the maximum expected cooperativity for P-1 can be estimated from the lifetime data via eq 4 to be $C_{max}^{P\text{-}1}=0.8 \pm 0.1$. Similarly for P-2, assuming the pure dephasing is of similar magnitude $(\gamma_d/2\pi \approx 506$ MHz), we estimate a cooperativity of $C^{P\text{-}2} \approx 0.35$, increasing to $C_{0\,K}^{P\text{-}2} \approx 0.45$ below the thermal-broadening limit, with a maximum value for a lifetime-limited line width of $C_{max}^{P\text{-}2} = 1.9 \pm 0.1$.

Although the SiV species studied here do not have lifetime-limited line widths, similar ranges of broadening were observed in other implanted SiV species that were not coupled to devices (SI.5). While this does not rule out that additional broadening mechanisms may have been introduced by the GaP itself (e.g., via charge traps or strain), it suggests that a sample with improved defect line widths could potentially achieve cooperativities $C > 1$ with little modification to the fabrication process. Monolithic diamond devices with similar cooperativities ($C = 1.6$) have recently been used to implement a quantum node,[40] indicating the potential for near-term exploration of quantum protocols in hybrid systems. Furthermore, relaxing the design limit on the minimum PhC hole dimension from $h_x = 70$ nm leads to an increase of Q by up to a factor of 10 for $h_x = 49$ nm (SI.9), thus indicating that $C \gtrsim 10$ can be achieved in hybrid device geometries despite the low refractive index contrast. This regime is promising for applications such as optical spin readout,[41] quantum-optical switches and tunable single-photon sources,[16] and quantum repeaters.[42]

In summary, we have demonstrated significant coupling between a GaP cavity and diamond SiV qubit avoiding all fabrication of the diamond substrate. Before integration the cavities can be characterized and tuned close to the specific target resonance wavelength. This enables optimization of the SiV−cavity coupling yield with the potential for minimal disruption to the qubit environment within the diamond. For the transferred GaP-on-diamond cavities, we measure quality factors close to the design target. Current device properties should enable cooperativity $C > 1$, with a promising outlook for $C \approx 10$ with modest design improvements. These results highlight the promise of hybrid photonic architectures for quantum network applications, even in relatively low-index contrast material combinations.

■ ASSOCIATED CONTENT

Supporting Information

The Supporting Information is available free of charge at https://pubs.acs.org/doi/10.1021/acs.nanolett.2c04890.

Schematic of microscope system, images of fabricated devices, room-temperature transmission spectra of GaP-on-diamond devices, tuning curves on different devices, resonant excitation measurements on both device and nondevice SiV, intensity dependence of SiV photoluminescence with 532 and 700 nm excitation, theory and simulation of the SiV−cavity system, fits and error approximation, and photonic crystal design and simulation (PDF)

■ AUTHOR INFORMATION

Corresponding Author

Nicholas S. Yama − *University of Washington, Electrical and Computer Engineering Department, Seattle, Washington 98105, United States;* orcid.org/0000-0002-6123-3313; Email: nsyama@uw.edu

Authors

Srivatsa Chakravarthi − *University of Washington, Physics Department, Seattle, Washington 98105, United States*

Alex Abulnaga − *Princeton University, Electrical and Computer Engineering Department, Princeton, New Jersey 08544, United States*

Ding Huang − *Princeton University, Electrical and Computer Engineering Department, Princeton, New Jersey 08544, United States; Institute of Materials Research and Engineering (IMRE), Agency for Science, Technology and Research (A*STAR), Singapore 138634, Singapore*

Christian Pederson − *University of Washington, Physics Department, Seattle, Washington 98105, United States*

Karine Hestroffer − *Department of Physics, Humboldt-Universitat zu Berlin, Berlin 10117, Germany*

Fariba Hatami − *Department of Physics, Humboldt-Universitat zu Berlin, Berlin 10117, Germany*

Nathalie P. de Leon − *Princeton University, Electrical and Computer Engineering Department, Princeton, New Jersey 08544, United States;* orcid.org/0000-0003-1324-1412

Kai-Mei C. Fu − *University of Washington, Physics Department, Seattle, Washington 98105, United States; University of Washington, Electrical and Computer Engineering Department, Seattle, Washington 98105, United States; Physical Sciences Division, Pacific Northwest National Laboratory, Richland, Washington 99352, United States*

Complete contact information is available at: https://pubs.acs.org/10.1021/acs.nanolett.2c04890

Author Contributions

S.C. and N.S.Y. contributed equally.

Notes

The authors declare no competing financial interest.

■ ACKNOWLEDGMENTS

This material is based upon work supported by Department of Energy, Office of Science, National Quantum Information Science Research Centers, Co-design Center for Quantum Advantage (C2QA), under contract number DE-SC0012704 and National Science Foundation Grant No. ECCS-1807566. N.S.Y. was supported by the National Science Foundation Graduate Research Fellowship Program under Grant No. DGE-2140004. A.A. was supported by a Post Graduate Scholarship from the Natural Sciences and Engineering Research Council of Canada (PGSD3-545932-2020). D.H. was supported by the National Science Scholarship from A*STAR, Singapore. The photonic devices were fabricated at the Washington Nanofabrication Facility, a National Nanotechnology Coordinated Infrastructure (NNCI) site at the University of Washington, which is supported in part by funds from the National Science Foundation (awards NNCI-2025489, 1542101, 1337840, and 0335765). The authors acknowledge the use of Princeton's Imaging and Analysis Center, which is partially supported through the Princeton Center for Complex Materials (PCCM), a National Science Foundation (NSF)-MRSEC program (DMR-2011750), as well as the Princeton Micro-Nano Fabrication Lab.

■ REFERENCES

(1) Ruf, M.; Wan, N. H.; Choi, H.; Englund, D.; Hanson, R. Quantum networks based on color centers in diamond. *J. Appl. Phys.* **2021**, *130* (7), 070901.

(2) Wehner, S.; Elkouss, D.; Hanson, R. Quantum internet: A vision for the road ahead. *Science* **2018**, *362* (6412), No. eaam9288.

(3) Kielpinski, D.; Monroe, C.; Wineland, D. J. Architecture for a large-scale ion-trap quantum computer. *Nature* **2002**, *417*, 709.

(4) Bassett, L. C.; Alkauskas, A.; Exarhos, A. L.; Fu, K.-M. C. Quantum defects by design. *Nanophotonics* **2019**, *8* (11), 1867−1888.

(5) Doherty, M. W.; Manson, N. B.; Delaney, P.; Jelezko, F.; Wrachtrup, J.; Hollenberg, L. C. The nitrogen-vacancy colour centre in diamond. *Phys. Rep.* **2013**, *528*, 1−45.

(6) Bradac, C.; Gao, W.; Forneris, J.; Trusheim, M. E.; Aharonovich, I. Quantum nanophotonics with group IV defects in diamond. *Nat. Commun.* **2019**, *10*, 5625.

(7) Radulaski, M.; Widmann, M.; Niethammer, M.; Zhang, J. L.; Lee, S.-Y.; Rendler, T.; Lagoudakis, K. G.; Son, N. T.; Janzén, E.; Ohshima, T.; Wrachtrup, J.; Vučković, J. Scalable Quantum Photonics with Single Color Centers in Silicon Carbide. *Nano Lett.* **2017**, *17*, 1782−1786.

(8) Miao, K. C.; Blanton, J. P.; Anderson, C. P.; Bourassa, A.; Crook, A. L.; Wolfowicz, G.; Abe, H.; Ohshima, T.; Awschalom, D. D. Universal coherence protection in a solid-state spin qubit. *Science* **2020**, *369* (6510), 1493−1497.

(9) Viitaniemi, M. L.; Zimmermann, C.; Niaouris, V.; D'Ambrosia, S. H.; Wang, X.; Kumar, E. S.; Mohammadbeigi, F.; Watkins, S. P.; Fu, K.-M. C. Coherent spin preparation of indium donor qubits in single zno nanowires. *Nano Lett.* **2022**, *22* (5), 2134−2139.

(10) Zhong, T.; Kindem, J. M.; Bartholomew, J. G.; Rochman, J.; Craiciu, I.; Miyazono, E.; Bettinelli, M.; Cavalli, E.; Verma, V.; Nam, S. W.; Marsili, F.; Shaw, M. D.; Beyer, A. D.; Faraon, A. Nanophotonic rare-earth quantum memory with optically controlled retrieval. *Science* **2017**, *357*, 1392−1395.

(11) Raha, M.; Chen, S.; Phenicie, C. M.; Ourari, S.; Dibos, A. M.; Thompson, J. D. Optical quantum nondemolition measurement of a single rare earth ion qubit. *Nat. Commun.* **2020**, *11* (1), 1−6.

(12) Huang, D.; Abulnaga, A.; Welinski, S.; Raha, M.; Thompson, J. D.; de Leon, N. P. Hybrid iii-v diamond photonic platform for quantum nodes based on neutral silicon vacancy centers in diamond. *Opt. Express* **2021**, *29*, 9174−9189.

(13) Lang, J.; Häußler, S.; Fuhrmann, J.; Waltrich, R.; Laddha, S.; Scharpf, J.; Kubanek, A.; Naydenov, B.; Jelezko, F. Long optical coherence times of shallow-implanted, negatively charged silicon vacancy centers in diamond. *Appl. Phys. Lett.* **2020**, *116* (6), 064001.

(14) Hepp, C.; Müller, T.; Waselowski, V.; Becker, J. N.; Pingault, B.; Sternschulte, H.; Steinmüller-Nethl, D.; Gali, A.; Maze, J. R.; Atatüre, M.; et al. Electronic structure of the silicon vacancy color center in diamond. *Phys. Rev. Lett.* **2014**, *112* (3), 036405.

(15) Sipahigil, A.; Jahnke, K.; Rogers, L.; Teraji, T.; Isoya, J.; Zibrov, A.; Jelezko, F.; Lukin, M. Indistinguishable Photons from Separated Silicon-Vacancy Centers in Diamond. *Phys. Rev. Lett.* **2014**, *113*, 113602.

(16) Sipahigil, A.; Evans, R. E.; Sukachev, D. D.; Burek, M. J.; Borregaard, J.; Bhaskar, M. K.; Nguyen, C. T.; Pacheco, J. L.; Atikian, H. A.; Meuwly, C.; et al. An integrated diamond nanophotonics platform for quantum-optical networks. *Science* **2016**, *354* (6314), 847−850.

(17) Bhaskar, M. K.; Riedinger, R.; Machielse, B.; Levonian, D. S.; Nguyen, C. T.; Knall, E. N.; Park, H.; Englund, D.; Lončar, M.; Sukachev, D. D.; Lukin, M. D. Experimental demonstration of memory-enhanced quantum communication. *Nature* **2020**, *580* (7801), 60−64.

(18) Levonian, D. S.; Riedinger, R.; Machielse, B.; Knall, E. N.; Bhaskar, M. K.; Knaut, C. M.; Bekenstein, R.; Park, H.; Lončar, M.; Lukin, M. D. Optical entanglement of distinguishable quantum emitters. *Phys. Rev. Lett.* **2022**, *128*, 213602.

(19) Cui, S.; Greenspon, A. S.; Ohno, K.; Myers, B. A.; Jayich, A. C. B.; Awschalom, D. D.; Hu, E. L. Reduced plasma-induced damage to near-surface nitrogen-vacancy centers in diamond. *Nano Lett.* **2015**, *15*, 2887−2891.

(20) Chakravarthi, S.; Pederson, C.; Kazi, Z.; Ivanov, A.; Fu, K.-M. C. Impact of surface and laser-induced noise on the spectral stability of implanted nitrogen-vacancy centers in diamond. *Phys. Rev. B* **2021**, *104* (8), 085425.

(21) Dibos, A.; Raha, M.; Phenicie, C.; Thompson, J. Atomic Source of Single Photons in the Telecom Band. *Phys. Rev. Lett.* **2018**, *120*, 243601.

(22) Barclay, P. E.; Fu, K.-M. C.; Santori, C.; Beausoleil, R. G. Chip-based microcavities coupled to nitrogen-vacancy centers in single crystal diamond. *Appl. Phys. Lett.* **2009**, *95*, 191115.

(23) Schmidgall, E. R.; Chakravarthi, S.; Gould, M.; Christen, I. R.; Hestroffer, K.; Hatami, F.; Fu, K.-M. C. Frequency Control of Single Quantum Emitters in Integrated Photonic Circuits. *Nano Lett.* **2018**, *18*, 1175−1179.

(24) Op de Beeck, C.; Haq, B.; Elsinger, L.; Gocalinska, A.; Pelucchi, E.; Corbett, B.; Roelkens, G.; Kuyken, B. Heterogeneous iii-v on silicon nitride amplifiers and lasers via microtransfer printing. *Optica* **2020**, *7* (5), 386−393.

(25) Heck, M. Inspire: Inp on sin photonic integrated circuits realized through wafer-scale micro-transfer printing. *Integrated Photonics Platforms II* **2022**, *12148*, 88−92.

(26) Billet, M.; Reis, L.; Léger, Y.; Cornet, C.; Raineri, F.; Sagnes, I.; Pantzas, K.; Beaudoin, G.; Roelkens, G.; Leo, F.; et al. Gallium phosphide-on-insulator integrated photonic structures fabricated using micro-transfer printing. *Optical Materials Express* **2022**, *12* (9), 3731−3737.

(27) Logan, A. D.; Shree, S.; Chakravarthi, S.; Yama, N.; Pederson, C.; Hestroffer, K.; Hatami, F.; Fu, K.-M. C. Triply-resonant sum frequency conversion with gallium phosphide ring resonators. *Opt. Express* **2023**, *31*, 1516−1531.

(28) Schneider, K.; Baumgartner, Y.; Hönl, S.; Welter, P.; Hahn, H.; Wilson, D. J.; Czornomaz, L.; Seidler, P. Optomechanics with one-dimensional gallium phosphide photonic crystal cavities. *Optica* **2019**, *6* (5), 577−584.

(29) Raha, M. *A Telecom-Compatible Quantum Memory in the Solid-State: Single Erbium Ions Coupled to Silicon Nanophotonic Circuits*. PhD thesis, Princeton University, 2021.

(30) Yablonovitch, E.; Hwang, D. M.; Gmitter, T. J.; Florez, L. T.; Harbison, J. P. Van der Waals bonding of GaAs epitaxial liftoff films onto arbitrary substrates. *Appl. Phys. Lett.* **1990**, *56*, 2419−2421.
(31) Chakravarthi, S.; Chao, P.; Pederson, C.; Molesky, S.; Ivanov, A.; Hestroffer, K.; Hatami, F.; Rodriguez, A. W.; Fu, K.-M. C. Inverse-designed photon extractors for optically addressable defect qubits. *Optica* **2020**, *7*, 1805.
(32) Huang, D. *Building Quantum Network Nodes Based on Neutral Silicon Vacancy Centers in Diamond*. PhD thesis, Princeton University, 2021.
(33) Turton, D. A.; Reid, G. D.; Beddard, G. S. Accurate analysis of fluorescence decays from single molecules in photon counting experiments. *Anal. Chem.* **2003**, *75*, 4182−4187.
(34) Jahnke, K. D.; Sipahigil, A.; Binder, J. M.; Doherty, M. W.; Metsch, M.; Rogers, L. J.; Manson, N. B.; Lukin, M. D.; Jelezko, F. Electron−phonon processes of the silicon-vacancy centre in diamond. *New J. Phys.* **2015**, *17* (4), 043011.
(35) Faraon, A.; Barclay, P. E.; Santori, C.; Fu, K.-M. C.; Beausoleil, R. G. Resonant enhancement of the zero-phonon emission from a colour centre in a diamond cavity. *Nat. Photonics* **2011**, *5* (5), 301−305.
(36) Purcell, E. M. Proceedings of the American physical society. *Phys. Rev.* **1946**, *69*, 674−674.
(37) Becker, J. N.; Becher, C. Coherence properties and quantum control of silicon vacancy color centers in diamond. *physica status solidi (a)* **2017**, *214* (11), 1700586.
(38) Neu, E.; Steinmetz, D.; Riedrich-Moller, J.; Gsell, S.; Fischer, M.; Schreck, M.; Becher, C. Single photon emission from silicon-vacancy colour centres in chemical vapour deposition nano-diamonds on iridium. *New J. Phys.* **2011**, *13*, 025012.
(39) Zhang, J. L.; Sun, S.; Burek, M. J.; Dory, C.; Tzeng, Y.-K.; Fischer, K. A.; Kelaita, Y.; Lagoudakis, K. G.; Radulaski, M.; Shen, Z.-X.; Melosh, N. A.; Chu, S.; Lončar, M.; Vučković, J. Strongly cavity-enhanced spontaneous emission from silicon-vacancy centers in diamond. *Nano Lett.* **2018**, *18*, 1360−1365.
(40) Stas, P.-J.; Huan, Y. Q.; Machielse, B.; Knall, E. N.; Suleymanzade, A.; Pingault, B.; Sutula, M.; Ding, S. W.; Knaut, C. M.; Assumpcao, D. R.; Wei, Y.-C.; Bhaskar, M. K.; Riedinger, R.; Sukachev, D. D.; Park, H.; Lončar, M.; Levonian, D. S.; Lukin, M. D. Robust multi-qubit quantum network node with integrated error detection. *Science* **2022**, *378* (6619), 557−560.
(41) Rogers, L. J.; Jahnke, K. D.; Metsch, M. H.; Sipahigil, A.; Binder, J. M.; Teraji, T.; Sumiya, H.; Isoya, J.; Lukin, M. D.; Hemmer, P.; et al. All-optical initialization, readout, and coherent preparation of single silicon-vacancy spins in diamond. *Physical review letters* **2014**, *113* (26), 263602.
(42) Dür, W.; Briegel, H.-J.; Cirac, J. I.; Zoller, P. Quantum repeaters based on entanglement purification. *Phys. Rev. A* **1999**, *59*, 169−181.